Molecular simulation of flow-enhanced nucleation in n-eicosane melts under steady shear and uniaxial extension

David A. Nicholson and Gregory C. Rutledge

Citation: The Journal of Chemical Physics **145**, 244903 (2016); doi: 10.1063/1.4972894

View online: http://dx.doi.org/10.1063/1.4972894

View Table of Contents: http://aip.scitation.org/toc/jcp/145/24

Published by the American Institute of Physics

Molecular simulation of flow-enhanced nucleation in *n*-eicosane melts under steady shear and uniaxial extension

David A. Nicholson and Gregory C. Rutledge
Department of Chemical Engineering, Massachusetts Institute of Technology, Cambridge, Massachusetts 02139, USA

(Received 28 October 2016; accepted 11 December 2016; published online 28 December 2016)

Non-equilibrium molecular dynamics is used to study crystal nucleation of *n*-eicosane under planar shear and, for the first time, uniaxial extension. A method of analysis based on the mean first-passage time is applied to the simulation results in order to determine the effect of the applied flow field type and strain rate on the steady-state nucleation rate and a characteristic growth rate, as well as the effects on kinetic parameters associated with nucleation: the free energy barrier, critical nucleus size, and monomer attachment pre-factor. The onset of flow-enhanced nucleation (FEN) occurs at a smaller critical strain rate in extension as compared to shear. For strain rates larger than the critical rate, a rapid increase in the nucleation rate is accompanied by decreases in the free energy barrier and critical nucleus size, as well as an increase in chain extension. These observations accord with a mechanism in which FEN is caused by an increase in the driving force for crystallization due to flow-induced entropy reduction. At high applied strain rates, the free energy barrier, critical nucleus size, and degree of stretching saturate, while the monomer attachment pre-factor and degree of orientational order increase steadily. This trend is indicative of a significant diffusive contribution to the nucleation rate under intense flows that is correlated with the degree of global orientational order in a nucleating system. Both flow fields give similar results for all kinetic quantities with respect to the reduced strain rate, which we define as the ratio of the applied strain rate to the critical rate. The characteristic growth rate increases with increasing strain rate, and shows a correspondence with the nucleation rate that does not depend on the type of flow field applied. Additionally, a structural analysis of the crystalline clusters indicates that the flow field suppresses the compaction and crystalline ordering of clusters, leading to the formation of large articulated clusters under strong flow fields, and compact well-ordered clusters under weak flow fields. *Published by AIP Publishing.* [http://dx.doi.org/10.1063/1.4972894]

I. INTRODUCTION

During the processing of crystallizable polymers, crystallization primarily occurs under conditions far from the ideal case, where quiescent, homogeneous nucleation predominates. Depending on the specifics of the crystallization conditions, the polymer melt is subjected to a variety of mechanical, thermal, and geometric factors, each of which has the capacity to alter the crystallization kinetics and resultant morphology of the material.[1] In particular, it has been widely observed that flow results in a dramatic increase in the rate of crystallization. This effect is ubiquitous in melt processing since it is difficult to conceive of a method for forming a polymer material that does not impart a deformation history.[2] Flow-induced crystallization (FIC) has been widely researched, yet there are still some consequential aspects of the process that are not held in consensus. In particular, there is little concrete knowledge about the earliest stage of FIC, sometimes referred to as flow-enhanced nucleation (FEN),[3] since it occurs at small spatiotemporal scales that are beyond the detection limit for even the most carefully constructed experiments.[4]

Under conditions that lead to polymer crystallization through the sporadic nucleation of stable crystalline clusters followed by deterministic growth, the evidence suggests that there exists a mechanism by which flow reduces the kinetic barrier to nucleation relative to that which is operative in the quiescent melt.[5] Numerous studies have shown that FIC is strongly dependent on the rheological behavior of the highest molecular weight chains in the melt.[5–8] This observation has given rise to the concept of precursors, which form during flow from perturbed high molecular weight chains and have an increased capacity to induce crystallization in a polydisperse melt upon cooling.[5,8] This manuscript focuses on nucleation from the monodisperse melt, and therefore the rheology of only the single length of chain present is important, and precursors are not expected to form.

The intensity of flow-enhanced effects depends on the capacity of the flow field to perturb molecules from their relaxed state. Meerveld *et al.* classified FIC behavior under shear based on the strain rate $\dot{\varepsilon}$ in terms of the reptation time τ_d and Rouse time τ_R of the melt.[7,9] They determined that there are three important ranges: (i) when $\dot{\varepsilon} < 1/\tau_d$, nucleation is effectively quiescent, (ii) when $1/\tau_d < \dot{\varepsilon} < 1/\tau_R$ the molecular orientation induces a modest increase in sporadic, isotropic nucleation, and (iii) when $\dot{\varepsilon} > 1/\tau_R$, the molecular stretching causes a drastic increase in the nucleation of oriented, fibrillar structures. This analysis indicated that chain stretching has the most dramatic effect, a result that has also been observed in continuum and meso-scale modelling.[10,11] The short chains used in this study do not entangle, and therefore the onset of

FEN effects is associated with τ_R. The Weissenberg number, $Wi = \dot{\varepsilon}\tau_R$, is a measure of the capacity of the flow field to perturb chains from their equilibrium conformations. The onset of flow-induced effects is expected to occur for $Wi \approx 1$.

The aforementioned difficulties associated with observing FEN experimentally have inspired modelling studies at a range of length-scales. Continuum models have proven effective for describing the later stages of FIC, including structure development and rheological properties.[7] At the mesoscale, Graham and Olmsted developed a coarse-grained kinetic Monte Carlo model that uses the GLaMM continuum rheological model[12] to sample chain configurations and adds segments of chains to a discretized nucleus using an acceptance criterion based on the segment-wise free energy.[5,11] Their model exhibited good agreement with experimental data, in support of the viewpoint that FEN can be explained by flow-induced entropy reduction in the melt; however, it must be considered to be a phenomenological model due to its rigid assumptions about the nucleus shape and its reliance on unknown thermodynamic parameters. At the molecular level, there have been simulation efforts using both Monte Carlo (MC)[13–15] and Molecular Dynamics (MD)[16–21] to study FIC; however, relatively few focused specifically on the kinetics of nucleation.[22] Given that nucleation is a transient event, a MC simulation cannot accurately capture its kinetics without an enormous amount of prior knowledge regarding the dynamic processes in the melt and their rates. For this reason, we believe that MD, which includes all of the classical physics of interacting particles, is the more attractive method for kinetic nucleation studies, where feasible, and directs readers to reviews that cover the application of MC methods to study FIC.[5,23]

Molecular dynamics studies of FIC have focused primarily on relatively short chains; long chains require both larger systems and longer times due to the strong molecular weight dependence of relaxation times. Furthermore, to date, these studies have been limited exclusively to alkanes, or oligo-ethylenes. Alkanes are referred to by the number of carbon atoms prefixed by "C." Koyama *et al.*[16,17] studied the crystallization of oriented C5000, prepared through cold-drawing below T_g then subsequently crystallized above T_g in the absence of an applied flow field. They observed rapid nucleation of oriented crystals, but were unable to distinguish nucleation and growth regimes. In a similar study by Ko *et al.*,[19] oriented samples were prepared by drawing under a constant, uniaxial load above T_m, then quenching below T_m in order to observe crystallization in the absence of an applied load. In these simulations, the nucleation and growth mechanism was observed, and found to result in rapid crystallization. Lavine *et al.*[24] studied the crystallization of chains ranging from C25 to C400 under uniaxial stress and a variety of thermal conditions. They found that when crystallization occurred under an applied uniaxial stress, nascent crystalline nuclei formed; however, their growth was suppressed. Jabbarzadeh and Tanner[20,21] performed constant-pressure, non-equilibrium molecular dynamics (NEMD) simulations of crystallization under shear and observed that steady shearing increases the crystallization rate for both C20 and C60 chains, and that pre-shearing increases the crystallization rate for C60 and longer C162 chains, but has no discernable effect for C20. Anwar *et al.*[22] performed constant-volume, NEMD studies of C20 and C150 under shear. Based on a mean first-passage time (MFPT) analysis, they identified a critical shear rate for the onset of rapid nucleation of oriented crystallites that corresponded reasonably well to the $Wi = 1$ condition. That study is the only one to date that provides quantitative information on the kinetics of FEN.

In this work, the kinetic mechanism of nucleation is investigated under both shear and, for the first time, uniaxial extensional flow, which is the relevant flow field for fiber formation. It is a commonly held assumption that flow increases the driving force for crystallization due to the melt entropy reduction associated with stretching and orienting chain molecules under flow, which, in turn, reduces the kinetic barrier to nucleation.[11,25–27] Although this concept has proven useful, it is difficult to demonstrate experimentally due to the inaccessibility of experimental measurements of the free energy barrier under flow. Using the simulation and analysis methods described in the manuscript, the free energy barrier under steady flow is computed, providing quantitative evidence for the flow-induced barrier reduction mechanism. The method makes use of NEMD simulation in order to observe nucleation under shear and uniaxial extension with varying strain rates. These observations are then used to parameterize a stochastic model of nucleation that is based on kinetic nucleation theory and valid for small nucleation barriers,[28] in order to determine the strain rate-dependencies of nucleation and growth rates and of critical kinetic parameters. By studying both planar shear and uniaxial extension, the effect of the type of applied flow field, in addition to its intensity, is discerned.

II. SIMULATION DETAILS

Simulations of flow-enhanced nucleation were performed using the non-equilibrium molecular dynamics (NEMD) method, in which the system is subjected to a constant flow field defined by the rate-of-deformation tensor $\nabla\mathbf{u}$, where $\mathbf{u}$ denotes the streaming velocity. The rate-of-deformation tensors for planar shear and uniaxial extensional flow fields are

$$\nabla\mathbf{u}_{\text{shear}} = \begin{bmatrix} 0 & \dot{\varepsilon} & 0 \\ 0 & 0 & 0 \\ 0 & 0 & 0 \end{bmatrix}, \quad \nabla\mathbf{u}_{\text{extension}} = \begin{bmatrix} \dot{\varepsilon} & 0 & 0 \\ 0 & -\dot{\varepsilon}/2 & 0 \\ 0 & 0 & -\dot{\varepsilon}/2 \end{bmatrix}. \quad (1)$$

The equations of motion under NEMD are the SLLOD equations,[29] which operate on the peculiar momentum of a particle, a quantity that is related to the lab frame velocity by $\mathbf{p}_i/m_i = \mathbf{v}_i - \mathbf{q}_i \cdot \nabla\mathbf{u}$,

$$\begin{aligned} \dot{\mathbf{q}}_i &= \frac{\mathbf{p}_i}{m_i} + \mathbf{q}_i \cdot \nabla\mathbf{u}, \\ \dot{\mathbf{p}}_i &= \mathbf{F}_i - \mathbf{p} \cdot \nabla\mathbf{u}. \end{aligned} \quad (2)$$

In addition to the equations of motion, NEMD simulations of homogeneous flow fields require boundary conditions that are compatible with the applied flow field. At each time point, homogeneity requires periodic boundary conditions in all 3 dimensions, and the simulation box serves as a basis for the lattice of periodic images of a particle located at the origin. As time evolves, the simulation box, and therefore the lattice of periodic images, must deform according to the applied

flow field. A compatible boundary condition is achieved when the simulation box defines a lattice that preserves a minimum spacing between periodic images of particles under the applied strain field.

Simulations of shear flow were performed using the Lagrangian rhomboid boundary condition,[30] which has been demonstrated to be equivalent[31] to the Lees-Edwards sliding brick boundary condition.[32] In this method, the initial simulation box is cubic, and upon deformation it evolves according to the three vectors:

$$\begin{aligned} \mathbf{h}_1(t) &= (1 \quad 0 \quad 0), \\ \mathbf{h}_2(t) &= (\varepsilon_{\text{box}}(t) \quad 1 \quad 0), \\ \mathbf{h}_3(t) &= (0 \quad 0 \quad 1). \end{aligned} \tag{3}$$

Since the simulation box is a basis for a lattice, for any applied strain $t\dot{\varepsilon}$ there are equivalent simulation boxes corresponding to $\varepsilon_{\text{box}}(t) = t\dot{\varepsilon} \pm k$ for $k \in \{0, 1, 2, \ldots\}$. In order to avoid a skewed simulation box, $\varepsilon_{\text{box}}(t)$ is restricted to the range $[-1/2, 1/2]$ using $\varepsilon_{\text{box}}(t) = t\dot{\varepsilon} - \lfloor t\dot{\varepsilon} \rceil$, where $\lfloor \cdot \rceil$ denotes the nearest integer function. This process of finding the least skewed simulation box for a given strain is equivalent to lattice reduction, which is the process of finding the least skewed basis for a given lattice.

Simulations of uniaxial extensional flow were performed using the method developed by Hunt.[33] In this method, the initial simulation box takes on a prescribed shape defined by the Vandermonde matrix of the roots of an irreducible cubic polynomial. Utilizing the same polynomial as Hunt, $\varphi^3 - 6\varphi^2 + 5\varphi - 1$, the initial simulation box is defined by its three roots, φ_1, φ_2, and φ_3,

$$\begin{aligned} \mathbf{h}_1(0) &= (1 \quad 1 \quad 1), \\ \mathbf{h}_2(0) &= (\varphi_1 \quad \varphi_2 \quad \varphi_3), \\ \mathbf{h}_3(0) &= \left(\varphi_1^2 \quad \varphi_2^2 \quad \varphi_3^2\right). \end{aligned} \tag{4}$$

As flow is applied, the simulation box deforms along with the flow field: $\mathbf{h}_i(t) = \mathbf{h}_i(0) \cdot \exp(t\nabla\mathbf{u})$. Using a result from number theory,[34] Hunt demonstrated that the lattice defined by $\mathbf{h}(t)$ preserves a minimum image distance upon any diagonal, traceless rate-of-deformation tensor, allowing simulations of uniaxial deformation to be performed for arbitrary duration. As is the case in shear, the initial simulation box becomes skewed upon applying uniaxial strain, and therefore lattice reduction should be performed to mitigate inefficient domain decomposition and loss of significance in arithmetical computations. The lattice reduction is not easily determined analytically as was the case in shear, requiring the application of a numerical lattice reduction algorithm throughout the simulation. For details, the reader is referred to the original paper by Hunt.[33] Another solution to the problem of lattice reduction for generalized, homogeneous flows in NEMD has been reported by Dobson.[35]

The uniaxial boundary conditions were implemented in the LAMMPS software package.[36] The LAMMPS requirement that the simulation box be expressed as an upper triangular matrix required a scheme in which the simulation system is repeatedly rotated between a non-upper triangular "flow frame," in which the positions and velocities of particles are updated according to the SLLOD equations, and a "LAMMPS frame," in which the remaining molecular dynamics routines were performed, including construction of neighbor lists and calculation of forces. Additionally, due to the exponential scaling of uniaxial deformation with strain, double precision arithmetic was insufficient for performing simulations at large strain. Following Hunt,[33] the arbitrary precision libraries GMP[37] and MPFR[38] were used for the computation of the box shape and the LLL algorithm,[39] as implemented in the fplll package,[40] was used for lattice reduction. In order to mitigate a known momentum instability in the SLLOD equations of motion under extension, the center of mass was periodically reset to zero every 100 timesteps.[31,33]

We have released the UEF package[41] for NEMD simulations of uniaxial flow in LAMMPS. This package is based on the method from Dobson,[35] which is equivalent to Hunt's method but possesses an implementation advantage since it does not require arbitrary precision libraries. The method implemented in UEF differs slightly from Dobson's in that it also utilizes numerical lattice reduction in order to find a fully reduced simulation box. The lattice reduction is performed using Semaev's algorithm[42] which, unlike the LLL algorithm, determines an optimally reduced basis according to the Minkowski criterion. It has been verified that Hunt's method,[33] used in this paper, and Dobson's method,[35] implemented in the UEF package, produce equivalent results for the stress response for a WCA fluid test system under uniaxial and biaxial extension. Additionally, both methods were found to yield the same stress response for a C20 system under uniaxial extension as a simulation with simply deforming boundary conditions, up until the point that the minimum image convention was violated in the simply deforming system.

In order to allow for the increase in density associated with crystallization, a constant-stress condition was imposed on one or more dimensions of the simulation box. The dimensions with constant stress were chosen to correspond to a free surface for typical laboratory flows. For shear, the stress was controlled in the vorticity direction, which would be exposed to atmospheric pressure in a cone-plate or plate-plate apparatus. For uniaxial extension, the stress was controlled in the compression directions, which correspond to free surfaces in fiber drawing. The stress condition in uniaxial extension is complicated by the boundary conditions, which require a specific box shape for a given level of strain. The desired stress conditions were achieved using a pressure control scheme in which the simulation box was scaled isotopically, but only the components of the pressure tensor in the compression directions were controlled to the target external pressure. For all simulations, the LAMMPS implementation of the Nose-Hoover thermostat and barostat was used, with time constants of 0.4 ps and 4 ps, respectively.

The simulated system and force field were the same as those used by Yi and Rutledge.[43,44] The system consisted of 336 C20 molecules, with a united atom (UA) representation in which each UA represents a CH_3 or CH_2 group. The force field was initially proposed by Paul, Yoon, and Smith[45] with subsequent modifications by Waheed *et al.*,[24,46] and includes bond stretching, bond angle bending, torsion, and non-bonded Lennard-Jones forces. The SLLOD equations of motion were integrated using a rRESPA scheme[47] with a time step of 2 fs for bonded interactions and 4 fs for intermolecular interactions.

Nucleation simulations were performed at 260 K (17% undercooling) and 1 atm for strain rates in the range of 10^7-10^9 s^{-1}, corresponding to Weissenberg numbers between 0.031 and 3.1 based on the 3.25 ns[43] Rouse time of C20 at 260 K for the force field used. At each strain rate, a melt was first equilibrated at 315 K under steady strain for 20 ns; at this temperature, the Weissenberg number was less than 1.0 (based on a Rouse time of 0.60 ns) for all strain rates. Equilibration was performed under steady straining in order to reduce the time required for the melt to adjust to the flow field upon quenching; nevertheless, transients in the melt structure upon quenching were unavoidable at the highest strain rates. From each equilibration trajectory, 40 snapshots were taken in intervals of 6 ns and quenched to 260 K in order to observe nucleation while maintaining the applied strain rate. The interval of 6 ns was chosen because it is roughly twice the Rouse time for C20.

III. ANALYSIS METHOD

For each nucleation run, crystalline clusters were determined using a method similar to the one proposed by Yi and Rutledge.[43] The local order parameter for each UA is defined according to

$$\langle P_2\rangle_{i,local} = \frac{1}{2}\left\langle 3\cos^2\theta_{ij} - 1\right\rangle_{j\in\Gamma_i}, \qquad \Gamma_i = \{k : \|\mathbf{r}_k - \mathbf{r}_i\| < r_{P2}, k \neq i, \mathrm{mol}_k \neq \mathrm{mol}_i\}. \tag{5}$$

In this expression, θ_{ij} is the angle between chord vectors located on atoms i and j, and the average for the ith UA is taken over all atoms within a distance r_{P2} that do not belong to the same molecule as i. Pairs of UAs belonging to the same molecule were excluded from the local order parameter in order to increase sensitivity to the intermolecular order associated with crystallization in systems under strong flow, which contain large populations of stretched chains. UAs that exceed a threshold value $P_{2,\mathrm{th}}$ for the local order parameter are eligible to form clusters of size greater than one. Eligible UAs are determined to be a part of the same cluster if they are within a threshold distance r_{th} of another eligible UA. All clusters of size one are considered to be in the monomer state, regardless of whether they exceeded the threshold value of $P_{2,\mathrm{th}}$. For this study the values $P_{2,\mathrm{th}} = 0.52$, $r_{P2} = 1.5\sigma_{lj}$, and $r_{\mathrm{th}} = 1.3\sigma_{lj}$ were used, where $\sigma_{lj} = 0.401$ nm is the van der Waals diameter of a CH_3 united atom. This results in a more local measure of orientational order as compared to our previous study,[28] which used $P_{2,\mathrm{th}} = 0.40$, $r_{P2} = 2.5\ \sigma_{lj}$, and $r_{\mathrm{th}} = 1.3\ \sigma_{lj}$ from Yi and Rutledge.[43] The smaller value of r_{P2} was chosen because it is more sensitive to fluctuations in orientational order associated with nucleation events for FEN simulations, which exhibit significant background orientation associated with the applied flow field. The value of $P_{2,\mathrm{th}}$ was chosen to detect similar cluster sizes for quiescent nucleation as the original choice from Yi and Rutledge.[43] In general, a large $P_{2,\mathrm{th}}$ value results in poor detection of small clusters, and a small $P_{2,\mathrm{th}}$ value results in the misclassification of slightly ordered, but non-crystalline, regions of the melt as crystalline clusters. For simulations of quiescent nucleation, the value used in this study yields similar MFPT curves, and therefore similar kinetic parameters including the free energy barrier and critical nucleus size, as our previous study.[28] In general, a small change in $P_{2,\mathrm{th}}$ results in a small change in the critical nucleus size, leaving the remaining kinetic parameters and steady-state rates largely unaffected. For each run, the size of the largest cluster in the system was monitored and the first-passage time curves $T_{\mathrm{largest,sim}}(1 \rightarrow n)$ were recorded as the earliest time that a cluster of size $\geq n$ was observed. The MFPT curve $\tau_{\mathrm{largest,sim}}(1 \rightarrow n)$ was found by averaging the first-passage times at each value of n for all 40 runs. The standard deviation curve $\sigma_{\mathrm{largest,sim}}(1 \rightarrow n)$ was computed from the sample variance of $T_{\mathrm{largest,sim}}(1 \rightarrow n)$ at each value of n.

The analysis of mean first-passage time data was performed using our recently reported method[28] for analyzing nucleation processes that exhibit small separation between time scales for nucleation and growth. In this method, first-passage time data from molecular simulation are fit to a stochastic nucleation model[48] in order to extract kinetic parameters and rates associated with the underlying nucleation process. Under the assumption of a constant cluster shape, the free energy $\Delta G(n)$ of forming a crystalline cluster of size n within the metastable melt follows the capillary approximation

$$\Delta G(n) = \Delta G^* \left[3\left(\frac{n^{2/3}-1}{(n^*)^{2/3}}\right) - 2\left(\frac{n-1}{n^*}\right)\right]. \tag{6}$$

The parameters ΔG^* and n^* are the free energy barrier and critical nucleus size, respectively. The formation of clusters is modeled using the Becker-Döring equations[49] for the time evolution of the cluster-size distribution function $C(n,t)$,

$$\frac{\partial C(1,t)}{\partial t} = 0,$$
$$\frac{\partial C(n,t)}{\partial t} = f(n-1)C(n-1,t) + g(n+1)C(n+1,t) - (f(n)+g(n))C(n,t). \tag{7}$$

The attachment rate, $f(n)$, is the rate at which a monomer is added to a cluster of size n, and it scales as the cluster surface area according to

$$f(n) = f_1 n^{\alpha}. \tag{8}$$

Under the assumption that the shape of a crystalline cluster is independent of cluster size, $\alpha = 2/3$. In preliminary studies of shear flow at 250 K, the surface area of the largest cluster was calculated based on the Voronoi tessellation, and α was found to lie in the range 0.69–0.74, which we considered close enough to 2/3 for subsequent analyses. The parameter f_1 is the monomer attachment pre-factor, and represents the average rate at which a labeled monomer forms a cluster of size 2. The detachment rate is specified by a stationary, or equilibrium, cluster distribution function that follows a Boltzmann distribution,

$$f(n)e^{-\beta\Delta G(n)} = g(n+1)e^{-\beta\Delta G(n+1)}. \tag{9}$$

For this model, the quantities ΔG^*, n^*, and f_1 completely determine the kinetics of a nucleating system. Following Gillespie,[48] it is assumed that for nucleation from a melt containing N total UAs, the first-passage time of the largest cluster is well-approximated by the first-passage time for the largest of N clusters evolving independently according to Eqs. (6)–(9).

This approximation leads to an expression for the MFPT of the largest cluster, $\tau_{\text{largest}}(1 \to n)$, based on the cumulative distribution function of the first-passage time for a single cluster, $F_T(t; 1 \to n)$,

$$\tau_{\text{largest}}(1 \to n) = \int_0^\infty (1 - F_T(t; 1 \to n))^N \, dt. \tag{10}$$

An approximation for the first-passage time distribution (FPTD) of a single cluster, based on its known hypoexponential structure,[50] provides an efficient and accurate route to computing $F_T(t; 1 \to n)$. The method requires the computation of the first i cumulants of the first-passage time, which are then used to approximate the slowest $i - 1$ rates of a hypoexponential distribution, as well as a time shift. As the number of cumulants i is increased, the accuracy of the FPTD increases. In this study, similar results were obtained using $i = 3$ and $i = 4$, and therefore the value of $i = 4$ was used for all fits to simulation data.

Estimates of the kinetic parameters ΔG^*, n^*, and f_1 are obtained from simulation data through a least squares fit to $\tau_{\text{largest}}(1 \to n)$, given in Eq. (10) and $\sigma_{\text{largest}}(1 \to n)$, which follows from the variance

$$\sigma^2_{\text{largest}}(1 \to n) = \int_0^\infty 2t\,(1 - F_T(t; 1 \to n))^N \, dt - \tau^2_{\text{largest}}(1 \to n). \tag{11}$$

The objective function for the fit is

$$Y(\Delta G^*, n^*, f_1) = \sum_{i=1}^{M} \Big[\big(\sigma_{\text{largest}}(1 \to i) - \sigma_{\text{largest,sim}}(1 \to i)\big)^2 + \big(\tau_{\text{largest}}(1 \to i) - \tau_{\text{largest,sim}}(1 \to i)\big)^2 \Big]. \tag{12}$$

The inclusion of the standard deviation in the fit is due to poor observed agreement between $\sigma_{\text{largest}}(1 \to n)$ and $\sigma_{\text{largest,sim}}(1 \to n)$ when only $\tau_{\text{largest}}(1 \to n)$ and $\tau_{\text{largest,sim}}(1 \to n)$ were used in the fitting procedure, in particular for analysis of simulation results at high strain rates. The inclusion of the standard deviation ensures that the parameterization of the stochastic model captures both the first and second-moment trends in first-passage times observed in simulations.

In addition to the parameters ΔG^*, n^*, and f_1, the stochastic model can also be used to determine kinetic rates. The steady-state nucleation rate is computed from

$$I_S = \rho_{n,\text{melt}} \left[\sum_{k=1}^{M} \frac{e^{\beta \Delta G(k)}}{f(k)} \sum_{j=1}^{k} e^{-\beta \Delta G(j)} \right]^{-1}. \tag{13}$$

The value M is the size of a large cluster that is highly unlikely to dissolve. Gillespie[48] demonstrated that the values $M = 2n^*$ and $M = 4n^*$ produced the same value for the nucleation rate. In this study, $M = 800$ was used for the computation of nucleation rates, as well as for the number of points in fits performed using Eq. (12), and was confirmed *a posteriori* to satisfy the condition: $M > 4n^*$. Under the assumption of a spherical nucleus, the characteristic growth rate is

$$G_S = \frac{f_1}{(36\pi \rho_{n,\text{xtal}})^{1/3}} \left(1 - \exp[-2\beta \Delta G^*/n^*]\right). \tag{14}$$

The quantities $\rho_{n,\text{melt}}$ and $\rho_{n,\text{xtal}}$ are the number density of UAs in the melt and crystal. The values used in this study were based on a melt density of 0.830 g cm^{-3} and crystal density of 0.936 g cm^{-3}, obtained by interpolation of the results of Yi and Rutledge[43] to 260 K.

IV. RESULTS

Fig. 1 shows the mean and standard deviation of the first-passage time of the largest cluster for nucleation of C20 under shear and extensional flow for a range of strain rates. The dramatic shift in $\tau_{\text{largest,sim}}(1 \to n)$ curves to smaller times with increasing strain rate indicates a strong FEN effect. Additionally, at low strain rates the $\tau_{\text{largest,sim}}(1 \to n)$ curves exhibit clear inflection points, whereas the curves at higher strain rates are comparatively featureless. This change in shape indicates that the free energy surface, and therefore the critical free energy barrier ΔG^* and critical nucleus size n^*, is affected

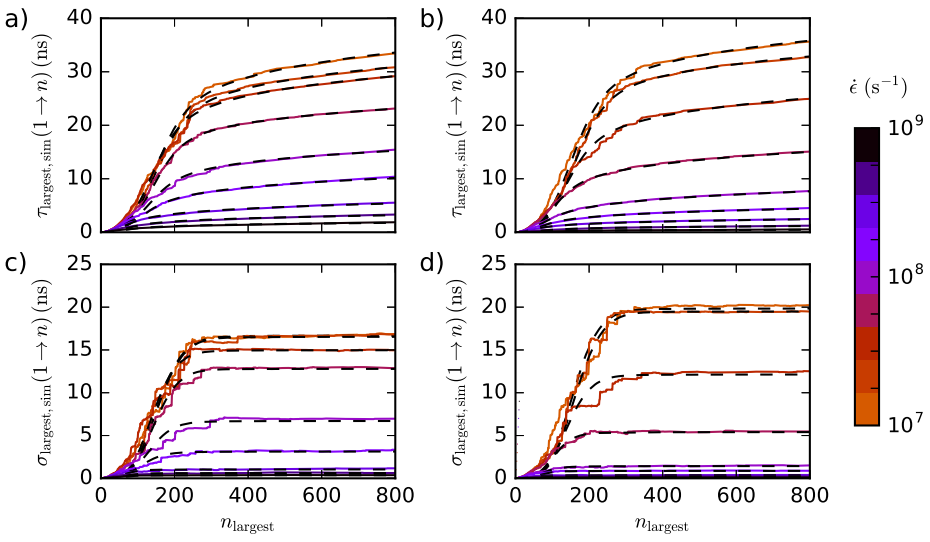

FIG. 1. Curves for the ((a) and (b)) mean and ((c) and (d)) standard deviation of the first-passage time of the largest cluster for nucleation of C20 under ((a) and (c)) shear and ((b) and (d)) extensional flow. The solid lines are data from MD simulation and the dashed lines are fits according to the objective function in Eq. (12). From top to bottom, the curves correspond to strain rates of 10^7 s^{-1}, $10^{7.25}$ s^{-1}, $10^{7.5}$ s^{-1}, $10^{7.75}$ s^{-1}, 10^8 s^{-1}, $10^{8.25}$ s^{-1}, $10^{8.5}$ s^{-1}, $10^{8.75}$ s^{-1}, $10^{9.0}$ s^{-1}.

by the intensity of the flow field, since a change in the monomer attachment pre-factor f_1 alone would not affect the shape of the curve. The $\sigma_{\text{largest,sim}}(1 \rightarrow n)$ curves, shown in Figs. 1(c) and 1(d), increase for small n before leveling off at large n. This trend is consistent with a nucleation and growth process in which the increase in $\sigma_{\text{largest,sim}}(1 \rightarrow n)$ is associated with the stochastic formation of a large supercritical cluster, and the subsequent leveling indicates that the growth of the supercritical cluster is deterministic. Following Shneidman,[51] the plateau value of the standard deviation σ_{plateau}, taken to be the average value of $\sigma_{\text{largest,sim}}(1 \rightarrow n)$ for $400 \leq n \leq 800$, can be used to compute an approximate steady-state nucleation rate for small systems, under the assumption that the FPTD is a shifted exponential,

$$I_S = \frac{\rho_{n,\text{melt}}}{N\sigma_{\text{plateau}}}. \tag{15}$$

The $\sigma_{\text{largest,sim}}(1 \rightarrow n)$ curves shift to smaller times with increasing strain rate, implying a dramatic increase in the nucleation rate according to Eq. (15).

The $\tau_{\text{largest,sim}}(1 \rightarrow n)$ and $\sigma_{\text{largest,sim}}(1 \rightarrow n)$ curves were fit to the stochastic nucleation model according to the objective function in Eq. (12). The fitted curves are shown as dashed lines in Fig. 1, and the resulting strain rate-dependent parameters are provided in Fig. 2 for both shear and extensional flow. The free energy barrier ΔG^* and critical nucleus size n^* exhibit similar trends with strain rate. Below a critical strain rate of $\dot{\epsilon}_c = 10^{7.75}\ \text{s}^{-1}$ for shear and $\dot{\epsilon}_c = 10^{7.25}\ \text{s}^{-1}$ for extension, both ΔG^* and n^* are effectively strain rate-independent. For strain rates above $\dot{\epsilon}_c$, ΔG^* and n^* decrease initially, then appear to saturate at high strain rates. The trends in ΔG^* and n^* are qualitatively similar in both shear and extension at the log-scale, with the main difference between them being the disparity in the critical strain rate. At high strain rates, where ΔG^* and n^* are relatively constant, the monomer attachment pre-factor f_1 increases dramatically. This increase indicates a significant diffusive contribution to the nucleation kinetics for strong flow fields.

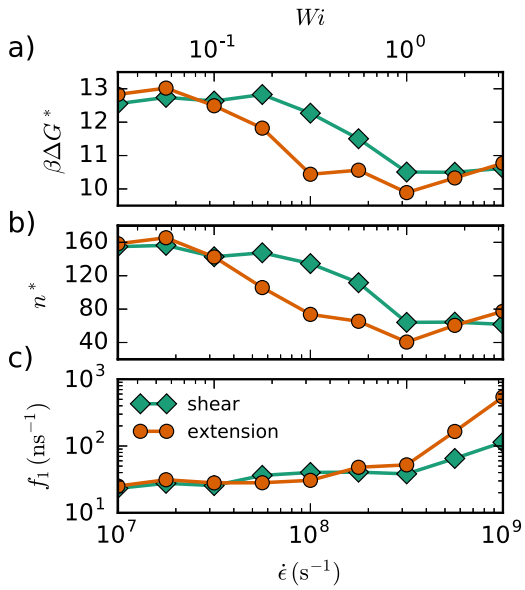

FIG. 2. Strain rate dependence of kinetic parameters for nucleation of C20 under shear and uniaxial extension: (a) the free energy barrier, (b) the critical nucleus size, and (c) the monomer attachment pre-factor. The top axis is the Weissenberg number based on the Rouse relaxation time for C20.

The steady-state nucleation rate I_S and characteristic growth rate G_S, computed from Eqs. (13) and (14), are the marked solid curves in Fig. 3. The nucleation rate estimate from Eq. (15) is the dashed curve in Fig. 3(a), and agrees well with the values from Eq. (13), suggesting that Shneidman's approximation[51] is in reasonable agreement with our analysis method[28] for the purposes of calculating this quantity, even when the energy barrier is diminished by flow. The nucleation rate exhibits a monotonic increase with strain rate above $\dot{\epsilon}_c$. As was the case for ΔG^* and n^*, the primary difference between the log-scale trends in nucleation rate under shear and extension is the disparity in the critical strain rate. Unlike ΔG^* and n^*, the nucleation rate does not saturate at high strain rates, at least within the range tested. The characteristic growth rate also increases with strain rates above $\dot{\epsilon}_c$, but the trend is less dramatic than the increase in I_S, and shifted slightly to higher strain rates.

In order to determine the effect of the flow field on chain configurations during the nucleation process, the root mean square (RMS) end-to-end distance $\left\langle R_{\text{ee}}^2 \right\rangle^{1/2}$, averaged over all chains, and the global nematic order parameter $\langle P_2 \rangle_{\text{global}} = \langle 3\cos^2\theta_{ij} - 1 \rangle_{i \neq j}/2$, averaged over all pairs of UAs in the system, were computed at each sampled time step for all nucleation runs. These quantities depend on the extent of crystallization, and therefore they have been computed as a function of the largest cluster size n_{largest}, binned into ranges of 20 UAs. Using this method, the effect of the flow field on chain conformations can be compared for systems with the same extent of crystallization.

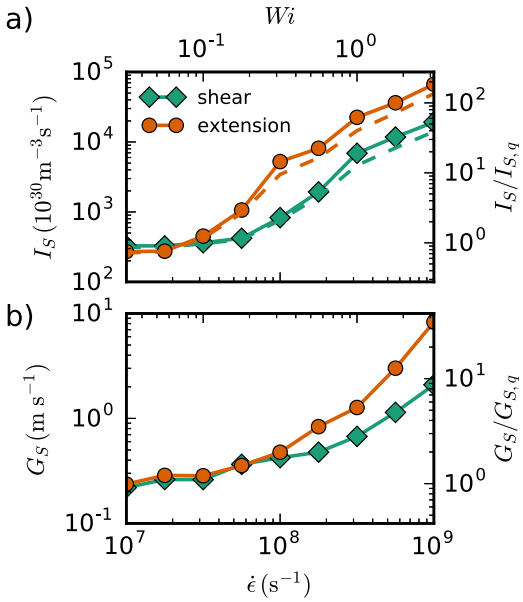

FIG. 3. Results for (a) steady-state nucleation rate and (b) steady-state characteristic growth rate for the nucleation of C20 under shear and uniaxial extension. The solid lines denote results obtained from fits to first-passage time data using (a) Eq. (13) and (b) Eq. (14). The dashed lines are the approximate nucleation rates from Eq. (15). The right axis scaling shows the flow-induced rate relative to (a) the quiescent nucleation rate $I_{S,q}$ and (b) quiescent growth rate $G_{S,q}$. The quiescent rate values can be found in our previous study.[28]

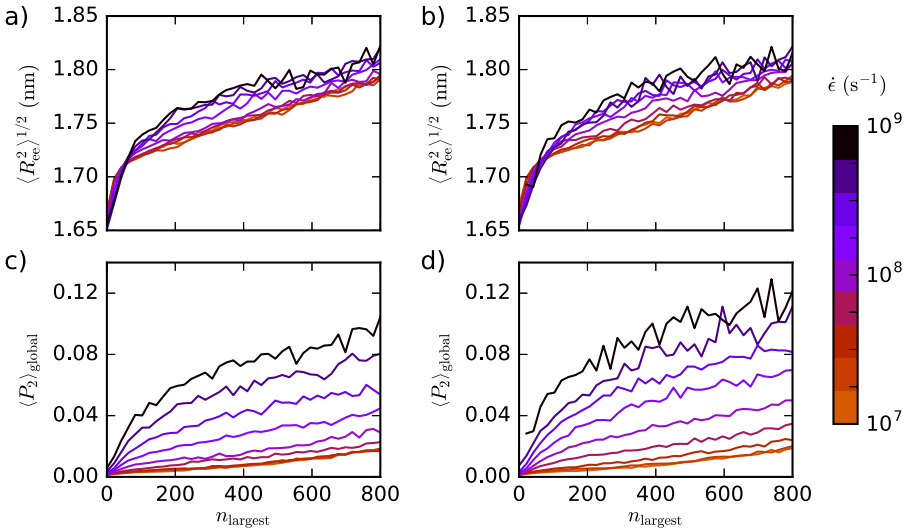

FIG. 4. Characterization of chain conformations during flow-enhanced nucleation, including the dependence of ((a) and (b)) the RMS end-to-end distance, and ((c) and (d)) the global nematic order parameter on size of the largest cluster for ((a) and (c)) shear and ((b) and (d)) uniaxial extensional flow.

At strain rates below the critical strain rate $\dot{\varepsilon}_c$, the RMS end-to-end distance curves, shown in Fig. 4(a) for shear and Fig. 4(b) for extension, exhibit similar trends with n_{largest}, indicating that the flow-field was not inducing extension of chains. As the strain rate was increased above $\dot{\varepsilon}_c$, the RMS end-to-end distance exhibited higher values, showing that chains were being extended by flow. While there is a clear difference between the curves at strain rates below and above $\dot{\varepsilon}_c$, it does not appear that the amount of extension caused by increasing the strain rate further above $\dot{\varepsilon}_c$ was very large, suggesting that other factors like orientational ordering may be more relevant. The global nematic order parameter is shown in Fig. 4(c) for shear and Fig. 4(d) for extension. As was the case for the RMS end-to-end distance, this nematic order parameter did not change drastically with strain rate below $\dot{\varepsilon}_c$. Above $\dot{\varepsilon}_c$, however, the nematic order parameter increased steadily with strain rate. It appears that increasing the strain rate above $\dot{\varepsilon}_c$ induces initially both orientation and extension of the chains in a nucleating system; however, increasing the strain rate further influences nucleation predominantly through a higher degree of orientation.

Characterization of the crystalline order of clusters formed during FEN was performed by measuring the nematic order parameter of the largest cluster $\langle P_2 \rangle_{\text{largest}}$, which was computed in a similar manner as $\langle P_2 \rangle_{\text{global}}$, but with the average taken only over pairs of atoms that belonged to the largest cluster. The dependence of $\langle P_2 \rangle_{\text{largest}}$ on the size of the largest cluster is shown for shear in Fig. 5(a) and extension in Fig. 5(b). The fractal dimension D_f was also computed using a box counting algorithm[52] that treats each UA as a sphere with diameter σ_{lj}. In this algorithm, a cubic volume containing the largest cluster was first identified with side length L, then subsequently divided into voxels with edge length $\delta = L/2, L/3$, etc. For each δ, the number of voxels that intersect with the spherical volume of any UA in the largest cluster were counted as $Q(\delta)$. The usual definition of the fractal dimension D_f derives from the scaling $Q(\delta) \sim \delta^{-D_f}$ as $\delta \to 0$. This definition is not suitable for analyzing the structure of clusters, however, since in the limit $\delta \to 0$, the value of $Q(\delta)$ exhibits the scaling of the compact spheres used to represent each UA. In this study, the fractal dimension D_f is defined as the slope of the curve $-\log Q(\delta)$ vs. $\log \delta$ for 1 nm $> \delta > \sigma_{lj}$. A perfectly compact object corresponds to $D_f = 3$, while smaller values correspond to less compact objects. The dependence of the fractal dimension on the size of the largest cluster is shown for shear in Fig. 5(c) and extension in Fig. 5(d).

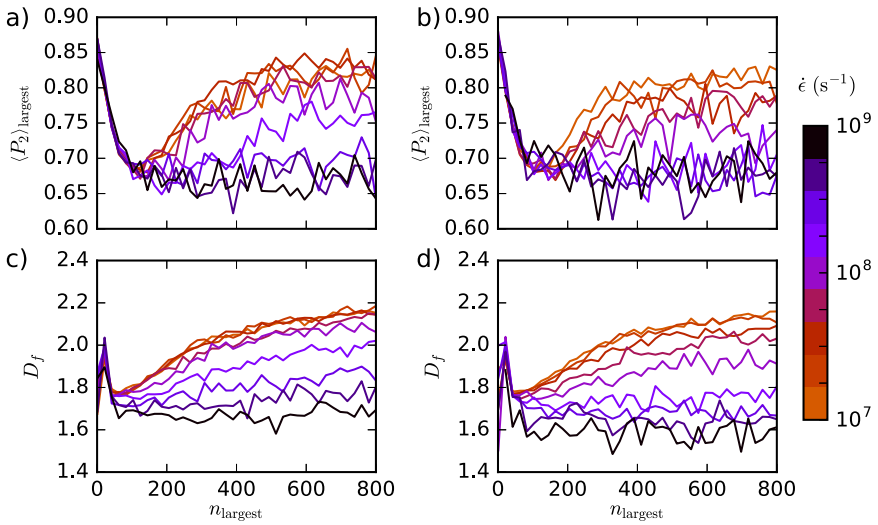

FIG. 5. Characterization of the structure of the critical nucleus, including the dependence of ((a) and (b)) the nematic order parameter of the largest cluster and ((c) and (d)) the fractal dimension of the largest cluster on the size of the largest cluster for ((a) and (c)) shear and ((b) and (d)) uniaxial extensional flow.

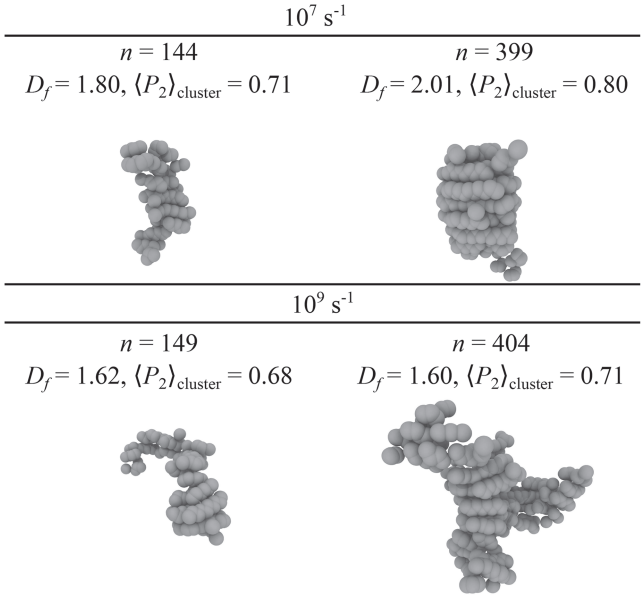

FIG. 6. Representative snapshots of small and large clusters under shear at 10^7 s^{-1} and 10^9 s^{-1}. The snapshots were selected based on their correspondence to the mean values of D_f and $\langle P_2 \rangle_{\text{largest}}$ associated with their size, shown in Fig. 5.

Based on Fig. 5, the structure of the largest cluster has a significant size dependence, even for low strain rates. For strain rates below $\dot{\varepsilon}_c$, small clusters have large orientational order; however, as the cluster size approaches the critical size n^*, the orientational order goes through a minimum and then subsequently increases with size for post-critical clusters. The fractal dimension exhibits a similar behavior, including a minimum near the critical cluster size, and a post-critical increase. These trends suggest that the critical nucleus is non-compact, and of intermediate orientational order, and that it is only with subsequent growth that a compact and well-ordered crystalline cluster is obtained. For strain rates above $\dot{\varepsilon}_c$, the orientational order and fractal dimension also decrease with the size of the largest cluster upon approaching the critical nucleus size. However, the post-critical ordering and compaction are inhibited by the applied flow field, resulting in the continued growth of large, articulated clusters. Representative snapshots of clusters at low and high shear rates are provided in Fig. 6 in order to provide insight into the effect of flow on the cluster structure. The snapshots were chosen based on their correspondence to the mean values of D_f and $\langle P_2 \rangle_{\text{largest}}$ associated with their size, based on the results shown in Figs. 5(a) and 5(c). These snapshots illustrate that for small clusters, both high and low shear rates lead to similar structures, however for large clusters, a low strain rate leads to more compact structures as compared to clusters formed under high shear rate.

V. DISCUSSION

The onset of flow-enhanced nucleation occurs at $Wi < 1$, and at different critical strain rates depending on the type of flow field. The values of the critical strain rate $\dot{\varepsilon}_c$ correspond to $Wi = 0.18$ in shear and $Wi = 0.056$ in extension based on the Rouse relaxation time of C20. These values are smaller than the critical strain rate expected for $Wi = 1$; however, some relevant rheological phenomena are already known to occur for $Wi < 1$. For example, dilute solution theory predicts a coil-stretch transition under extensional flow at $Wi = 0.5$ based on the Zimm relaxation time.[53] The shear value is in reasonable agreement with Anwar *et al.*[22] who observed the onset of FEN at $Wi = 0.6$ based on the center of mass diffusion time of a C20 molecule, rather than the Rouse relaxation time. The smaller critical strain rate $\dot{\varepsilon}_c$ observed under extension as compared to shear is likely due to the greater capacity for extensional flow to orient and stretch molecules, a phenomenon that has been observed in dilute solutions,[54] and can be observed in Fig. 4, in particular for strain rates near $\dot{\varepsilon}_c$.

The trends toward decreasing free energy barrier ΔG^* and critical nucleus size n^* as functions of increasing strain rate, shown in Fig. 2, are consistent with a mechanism in which the entropy-driven increase in free energy associated with stretching and orientation of the melt under flow results in a higher driving force ΔG_b for nucleation, since the free energy barrier and critical nucleus size depend inversely on the driving force under the assumption of constant surface tension,

$$\Delta G^* \propto \Delta G_b^{-2} \quad n^* \propto \Delta G_b^{-3}. \tag{16}$$

The decrease in the critical nucleus size n^* with increasing strain rate observed here conflicts with the results of Anwar *et al.*[22] for start-up shear, who observed no significant trend in the critical nucleus size with strain rate for C20 nucleation at 250 K. This discrepancy may be due to a different dependence of the critical nucleus size on strain rate in start-up flow, as compared to steady-state flow. However, flow-induced stretching and orientation of chain molecules should occur in both start-up and steady-state flow, and the associated entropy reduction should lead to a decrease in the critical nucleus size for both flow conditions. More likely, this discrepancy is due to their choice of method for the analysis of MFPT data. In their study, the method from Wedekind *et al.*[57] was used, which is only valid in the limit of large free energy barrier and small system size. In our recent study,[28] the assumptions of Wedekind *et al.* were examined and found not to hold at short times for quiescent nucleation of C20, even using a system that was smaller, and at shallower undercooling, than that of Anwar *et al.*[22] Under flow, we expect that the further reduction in free energy barrier would result in conditions that make these assumptions increasingly inappropriate.

Another possible source of discrepancy is finite-size effects, which cannot be completely discounted. However, the simulation box used is large enough to accommodate 2 fully extended C20 molecules in each dimension, and only clusters of size ≤800 UAs were included in the MFPT analysis, corresponding to <12% of the system; the computed critical nucleus sizes correspond to <3% of the system. In an umbrella sampling study of *n*-octane nucleation at 20% undercooling, there was no difference in the computed free energy curves for a small system for which the critical nucleus corresponded to 4.2% of the total system and a large system for which the critical nucleus comprised 2.1%.[55] Given that the critical nucleus falls within the same range of this study, it seems unlikely that finite-size effects are significant herein. In any case, finite-size effects due to small system size would lead to an overestimate of the nucleation rate, and underestimates of the free

energy barrier and critical nucleus size. As the driving force for crystallization increases, the magnitude of the bias associated with finite-size effects decreases.[56] Taken together, these trends suggest that any bias due to finite size effects in the estimation of I_S, ΔG^*, and n^* shown in Figs. 3 and 4 would only serve to underestimate the true magnitude of changes with increasing strain rate.

At high strain rates, ΔG^* saturates to values in the range of 10-11 kT, and n^* to values in the range 40-80. A similar trend is present in the RMS end-to-end distance $\left\langle R_{ee}^2 \right\rangle^{1/2}$, which shows an initial increase upon exceeding the critical strain rate, but does not show a strong strain rate dependence at large strain rate. This is an indication that the decrease in the free energy barrier is primarily associated with flow-induced extension, as opposed to the global orientational order, which increases steadily with strain rate. The monomer attachment pre-factor, on the other hand, continues to increase with strain rate above $\dot{\varepsilon}_c$, which is an indication that there is a significant diffusive contribution to the nucleation kinetics under steady-state flow. This diffusive contribution is correlated with the increase in the global orientational order, and appears to reflect an increase in the likelihood of collisions leading to cluster formation in a system with a greater degree of orientational order.

Based on Figs. 2 and 3, the trends in both kinetic parameters and steady-state nucleation and growth rates exhibit similar logarithmic trends above the critical strain rate. To investigate this observation further, the data in Figs. 2 and 3 are replotted versus the reduced strain rate $\dot{\varepsilon}/\dot{\varepsilon}_c$ in Figs. 7 and 8, where the critical strain rate in shear is about 3.2 times that in uniaxial extension. Upon this transformation, the trends in ΔG^*, n^*, f_1, I_S, and G_S collapse reasonably well to master curves.

The acceleration in the nucleation rate under shear, shown in Fig. 3, is more dramatic than that observed by Anwar *et al.*[22] at deeper undercooling. Over the strain rate range of 10^7-10^9 s^{-1}, we see an increase in the nucleation rate by a factor of 80, whereas they observed an increase by a factor of roughly 10. We speculate that this discrepancy may be attributable to a weaker FEN effect at deep undercooling, but differences in simulation conditions and analysis method may also be responsible. In particular, their study was for start-up shear, whereas steady-state shear was used in this study. Compared to the nucleation rate, the effect of flow on the growth rate is less well-studied in the literature; however, studies of shear-induced crystallization of iPP[58] have shown an increase in the growth rate of spherulites with increasing shear rate, in agreement with our results. These studies also found that the measured nucleation rate exhibited a power law correlation with the growth rate over a range of different crystallization temperatures and applied strain rates (cf. Fig. 12 of Pantani *et al.*[58]). In Fig. 9 the steady-state nucleation rate is plotted against the growth rate, under both shear and extension. Collapse of these relations onto the same curve indicates that accelerations in the nucleation rate and the growth rate are correlated similarly under different applied flow fields. At high nucleation and growth

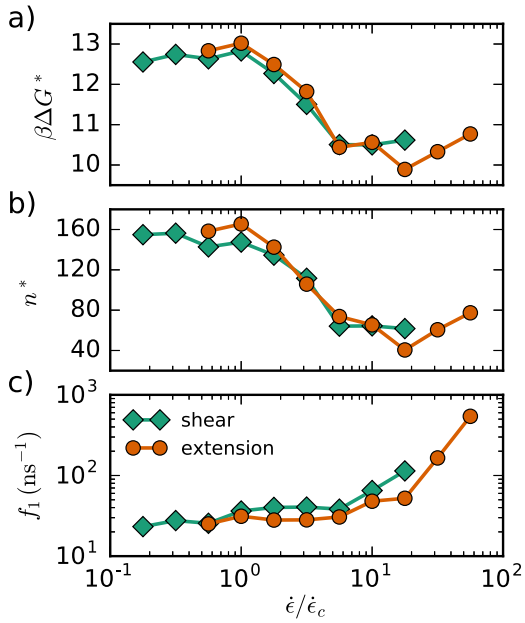

FIG. 7. Simulation data from Fig. 2, plotted as functions of the reduced strain rate, instead of the absolute strain rate.

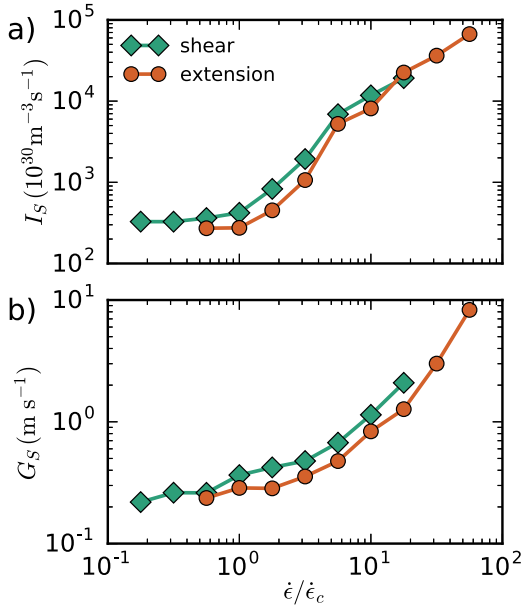

FIG. 8. Simulation data from Fig. 3, plotted as functions of the reduced strain rate, instead of absolute strain rate.

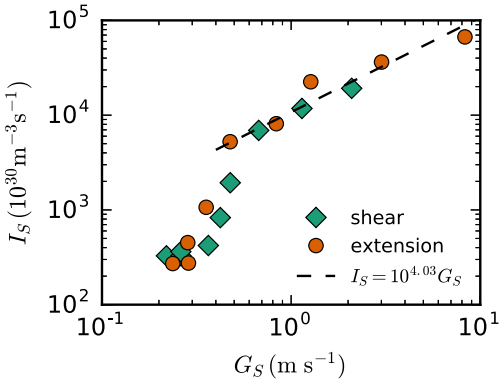

FIG. 9. Correlation of the steady-state nucleation rate and characteristic growth rate for flow-induced crystallization of C20. Each point corresponds to a different applied shear or extension rate. The dashed line is a linear fit for strain rates with $\dot{\varepsilon}/\dot{\varepsilon}_c > 5$, corresponding to saturation of ΔG^* and n^*.

rates, I_S and G_S are linearly proportional to one another. The onset of linear proportionality coincides with the saturation in ΔG^* and n^* at high strain rate. This behavior is due to the linear dependence of both the nucleation rate and the growth rate on f_1. As a result of this dependence, when ΔG^* and n^* are constant, I_S and G_S are linearly proportional.

In addition to the effects of flow on the kinetic parameters and steady-state rates associated with nucleation and growth, the applied flow field was also found to affect the structure of the clusters formed. Irrespective of the applied flow field, the nucleation process was characterized by the initial formation of a non-compact critical cluster with intermediate orientational order. For strain rates below $\dot{\varepsilon}_c$, the growth of the critical cluster to large size was accompanied by the compaction and ordering of the cluster. For strain rates above $\dot{\varepsilon}_c$, however, the post-critical compaction and ordering of the cluster were inhibited, resulting in the growth of large, articulated clusters. This effect is likely caused by the requirement that the cluster accommodate the stress due to the flow field. Under an affine deformation field, adjacent chains slide past one another. When a cluster is formed under flow, chains resist this affine sliding and, as a result, are subject to a stress. This stress increases as the thickness of the cluster increases in directions corresponding to large velocity gradients. Due to the anisotropy of the applied flow field, the cluster tends to maintain small dimensions in these directions to avoid large stresses, resulting in articulated, rather than compact, structures.

VI. CONCLUSIONS

Flow enhanced nucleation studies were carried out under steady-state shear and uniaxial extension using NEMD. As a result of these studies, the effect of flow on the kinetic parameters associated with nucleation was established, as well as the steady-state rates of nucleation and growth. Across the different flow conditions, a universal behavior emerged, characterized by the reduced strain rate $\dot{\varepsilon}/\dot{\varepsilon}_c$, where $\dot{\varepsilon}_c$ is the critical strain rate for the onset of FEN for a given flow field. At small reduced strain rates ($\dot{\varepsilon}/\dot{\varepsilon}_c < 1$), the nucleation kinetics were effectively the same as for quiescent nucleation. For intermediate reduced strain rates ($1 < \dot{\varepsilon}/\dot{\varepsilon}_c < 5$), the nucleation kinetics accelerated in a manner consistent with an entropy-driven increase in the flow-induced driving force for crystallization. At large reduced strain rates ($\dot{\varepsilon}/\dot{\varepsilon}_c > 5$), the additional increase in the nucleation kinetics was attributed to a diffusive contribution.

Both the steady-state nucleation rate and the characteristic growth rate were found to increase dramatically due to the applied flow field. Furthermore, a correlation between the nucleation rate and growth rate was observed across both shear and extensional nucleation studies. This correlation suggests that existing experimental results that exhibit a similar correlation across varying thermal and shear conditions may be extended to include crystallization under extensional flow as well.

Connections were established between the molecular conformations in the nucleating melt, and related effects on the nucleation kinetics. The degree of stretching was found to correlate with kinetic parameters associated with the flow-induced driving force for crystallization, indicating that it is primarily stretching rather than orientation that is characteristic of the flow-induced reduction of melt entropy. The degree of orientation was found to correlate with kinetic parameters associated with the diffusive contribution to flow-enhanced nucleation, indicating that a well-oriented melt leads to greater frequencies of monomer-monomer collisions that form clusters.

In addition to kinetic effects, flow was found to have a strong influence on the structural development of clusters. Independent of strain rate, sub-critical clusters were found to grow at the expense of orientational order and compactness. For small strain rates, ordering and compaction were observed upon growth of the critical cluster to large size. Under large strain rates, however, the post-critical ordering and compaction was suppressed, resulting in the growth of large articulated clusters.

ACKNOWLEDGMENTS

Financial support was provided by the ExxonMobil Research and Engineering Company. We are grateful to Dr. Rebecca Locker for helpful discussions.

[1] J.-M. Haudin, in *Handbook of Polymer Crystallization*, edited by E. Piorkowska and G. C. Rutledge (Wiley, Hoboken, 2013), pp. 433–462.
[2] H. Janeschitz-Kriegl, *Crystallization Modalities in Polymer Melt Processing* (Springer Vienna, Vienna, 2010).
[3] P. C. Roozemond, R. J. A. Steenbakkers, and G. W. M. Peters, Macromol. Theory Simul. **20**, 93 (2011).
[4] J. Baert and P. Van Puyvelde, Macromol. Mater. Eng. **293**, 255 (2008).
[5] R. S. Graham, Chem. Commun. **50**, 3531 (2014).
[6] G. Kumaraswamy, J. Macromol. Sci., Polym. Rev. **45**, 375 (2005).
[7] G. W. M. Peters, L. Balzano, and R. J. A. Steenbakkers, in *Handbook of Polymer Crystallization*, edited by E. Piorkowska and G. C. Rutledge (Wiley, Hoboken, 2013), pp. 399–431.
[8] G. Lamberti, Chem. Soc. Rev. **43**, 2240 (2014).
[9] J. van Meerveld, G. W. M. Peters, and M. Hütter, Rheol. Acta **44**, 119 (2004).
[10] R. J. A. Steenbakkers and G. W. M. Peters, J. Rheol. **55**, 401 (2011).
[11] R. S. Graham and P. D. Olmsted, Phys. Rev. Lett. **103**, 115702 (2009).
[12] R. S. Graham, A. E. Likhtman, T. C. B. McLeish, and S. T. Milner, J. Rheol. **47**, 1171 (2003).
[13] W. Hu, D. Frenkel, and V. B. F. Mathot, Macromolecules **35**, 7172 (2002).
[14] C. Baig and B. J. Edwards, Europhys. Lett. **89**, 36003 (2010).
[15] Y. Nie, H. Gao, M. Yu, Z. Hu, G. Reiter, and W. Hu, Polymer **54**, 3402 (2013).
[16] A. Koyama, T. Yamamoto, K. Fukao, and Y. Miyamoto, J. Macromol. Sci., Part B **42**, 821 (2003).
[17] A. Koyama, T. Yamamoto, K. Fukao, and Y. Miyamoto, Phys. Rev. E **65**, 50801 (2002).
[18] M. S. Lavine, N. Waheed, and G. C. Rutledge, Polymer **44**, 1771 (2003).
[19] M. J. Ko, N. Waheed, M. S. Lavine, and G. C. Rutledge, J. Chem. Phys. **121**, 2823 (2004).
[20] A. Jabbarzadeh and R. I. Tanner, J. Non-Newtonian Fluid Mech. **160**, 11 (2009).
[21] A. Jabbarzadeh and R. I. Tanner, Macromolecules **43**, 8136 (2010).
[22] M. Anwar, J. T. Berryman, and T. Schilling, J. Chem. Phys. **141**, 124910 (2014).
[23] G. C. Rutledge, in *Handbook of Polymer Crystallization*, edited by E. Piorkowska and G. C. Rutledge (Wiley, Hoboken, 2013), pp. 197–214.
[24] N. Waheed, M. S. Lavine, and G. C. Rutledge, J. Chem. Phys. **116**, 2301 (2002).
[25] S. Acierno, S. Coppola, N. Grizzuti, and P. L. Maffettone, Macromol. Symp. **185**, 233 (2002).
[26] S. Coppola, N. Grizzuti, and P. L. Maffettone, Macromolecules **34**, 5030 (2001).
[27] R. Zheng and P. K. Kennedy, J. Rheol. **48**, 823 (2004).
[28] D. A. Nicholson and G. C. Rutledge, J. Chem. Phys. **144**, 134105 (2016).

[29]D. J. Evans and G. P. Morriss, *Statistical Mechanics of Nonequilibrium Liquids* (Academic, London, 1990).
[30]D. J. Evans, Mol. Phys. **37**, 1745 (1979).
[31]T. A. Hunt and B. D. Todd, Mol. Phys. **101**, 3445 (2003).
[32]A. W. Lees and S. F. Edwards, J. Phys. C: Solid State Phys. **5**, 1921 (1972).
[33]T. A. Hunt, Mol. Simul. **42**, 347 (2015).
[34]H. Davenport, Proc. London Math. Soc. **2**, 412 (1938).
[35]M. Dobson, J. Chem. Phys. **141**, 184103 (2014).
[36]S. Plimpton, J. Comput. Phys. **117**, 1 (1995).
[37]T. Granlund, Computer Program GNU MP, http://gmplib.org, 2012.
[38]L. Fousse, G. Hanrot, V. Lefèvre, P. Pélissier, and P. Zimmermann, ACM Trans. Math. Software **33**, 13 (2007).
[39]A. K. Lenstra, H. W. Lenstra, and L. Lovász, Math. Ann. **261**, 515 (1982).
[40]M. Albrecht, S. Bai, D. Cadé, X. Pujol, and D. Stehlé, Computer Program FPLLL, https://github.com/fplll/fplll, 2014.
[41]D. A. Nicholson, Computer Program UEF, https://github.com/RutledgeGroupMIT/UEF, 2016.
[42]I. Semaev, in *Cryptography and Lattices*, edited by J. H. Silverman (Springer, Berlin, Heidelberg, 2001), pp. 181–193.
[43]P. Yi and G. C. Rutledge, J. Chem. Phys. **135**, 24903 (2011).
[44]P. Yi, C. R. Locker, and G. C. Rutledge, Macromolecules **46**, 4723 (2013).
[45]W. Paul, D. Y. Yoon, and G. D. Smith, J. Chem. Phys. **103**, 1702 (1995).
[46]N. Waheed, M. J. Ko, and G. C. Rutledge, Polymer **46**, 8689 (2005).
[47]M. E. Tuckerman, B. J. Berne, and G. J. Martyna, J. Chem. Phys. **97**, 1990 (1992).
[48]D. T. Gillespie, J. Chem. Phys. **74**, 661 (1981).
[49]R. Becker and W. Döring, Ann. Phys. **416**, 719 (1935).
[50]S. Karlin and J. McGregor, Pacific J. Math. **9**, 1109 (1959).
[51]V. A. Shneidman, J. Chem. Phys. **141**, 51101 (2014).
[52]J. J. Gagnepain and C. Roques-Carmes, Wear **109**, 119 (1986).
[53]R. G. Larson and J. J. Magda, Macromolecules **22**, 3004 (1989).
[54]D. E. Smith, H. P. Babcock, and S. Chu, Science **283**, 1724 (1999).
[55]P. Yi and G. C. Rutledge, J. Chem. Phys. **131**, 134902 (2009).
[56]J. Wedekind, D. Reguera, and R. Strey, J. Chem. Phys. **125**, 214505 (2006).
[57]J. Wedekind, R. Strey, and D. Reguera, J. Chem. Phys. **126**, 134103 (2007).
[58]R. Pantani, I. Coccorullo, V. Volpe, and G. Titomanlio, Macromolecules **43**, 9030 (2010).